

Multi-objective analysis of the Sand Hypoplasticity model calibration

Francisco J. Mendez^{1,*}, Miguel A. Mendez², Nicola Sciarra¹, Antonio Pasculli¹

¹University G. D'Annunzio, Dept. of Engineering Geology (INGEO), Chieti-Pescara, Italy;

² von Karman Institute for Fluid Dynamics, EA Department, Sint-Genesius-Rode, Belgium

*Corresponding to: francisco.mendez@unich.it

Abstract

The Sand Hypoplastic (SH) constitutive law by von Wolffersdorff (1996) is an interesting hypoplastic model for soil mechanics. This model includes eight parameters, usually calibrated using the oedometric (OE) and the drained isotropically consolidated triaxial tests (CD). However, previous studies show that the SH model calibration in the CD test has conflicting requirements in predicting the evolution of stresses and strains.

In this work, we study the SH model calibration over a wide range of testing conditions using 12 OE and 25 CD tests by Wichtmann and Triantafyllidis (2016) on the Karlsruhe sands. The parameter space is extensively explored via Genetic Algorithm Optimization (GA) using the recently developed open-source software GA-cal (available at <https://github.com/FraJoMen/GA-cal>). This exploration allowed us to study the SH model's predictive limits and to identify, using a multi-objective analysis, the main parameters governing the compromise between the accurate prediction of stresses versus strain in the CD tests.

Keywords Automatic calibration, Hypoplasticity, Numerical optimization, Genetic Algorithm, Nonlinear Regression

1. Introduction

Based on the first Hypoplastic constitutive law [44], several models have been developed to describe the stress-strain behaviour of clay [39, 40, 21, 19, 20] and sand [45, 6, 43, 9, 1], with extensions available for cyclic loads [27, 5, 35, 7]. Arguably one of the most famous hypoplastic model is the one proposed by von Wolffersdorff [37], often referred to as Sand Hypoplasticity (SH). This model has been successfully applied to a wide variety of problems in geotechnical engineering [38, 18, 32], despite its limitations [45].

The SH model requires eight parameters. These are traditionally calibrated from geotechnical laboratory tests, as firstly proposed in [10]. The early approaches for the SH model calibration, however, relied on a large number of laboratory tests and estimates of the tangents to the response

curves. Unfortunately, such estimates are usually impossible in some tests (e.g. in the oedometric curves) because of the coarse time-stepping, and are particularly sensitive to measurement noise in others (e.g. in the triaxial tests). Moreover, the formulas used to compute the model parameters are extremely sensitive to the input data, resulting in considerable uncertainties in the estimated parameters and the need for non-trivial manual adjustments to improve the model predictions.

To reduce the manual adjustments in the SH calibration, a more robust approach has been proposed in [12, 13, 33, 34] and made available in the free software ExCalibre (www.soilmodels.com/excalibre). This approach solely relies on experimental data from the oedometric (OE) and drained isotropically consolidated triaxial tests (CD) tests and uses a combination of empirical relations and optimization. Interestingly, this approach ignores the SH model predictions of the volumetric strain and uses the OE data to calibrate some of the parameters and the CD data to calibrate others. This is a convenient but restrictive simplification because all parameters play a role in determining the soil response in both tests.

More general methods formulating the calibration of constitutive laws as a regression problem were proposed in [49, 46, 47]. The regression solution involves an optimization, for which both deterministic and stochastic approaches have been proposed, as reviewed in [12] and [13].

Stochastic Optimisers (SO) are notoriously less sample efficient than deterministic ones (see [29]) but allow for better exploring the parameter space without being trapped in local minima. These optimisers are based on the generation of pseudorandom numbers commonly used by the Monte Carlo method, which has also been applied in different fields in [3, 30, 31, 26]. The most popular SO used in the parameter calibration of a constitutive model are the genetic algorithm (GA) [28, 11, 16, 48, 52], the differential evolution [36, 51, 17], and particle swarm optimisation [15, 2, 50]. The authors recently proposed the first calibration of SH using GA in [25]. In this work, the GA was proven able to provide a good calibration and was also employed to quantify the model prediction's sensitivity, the model parameters' un-

certainty and the potential correlations between them.

The availability of powerful optimization techniques and ever-increasing experimental datasets allows for exploring and stretching the SH model’s predictive capabilities. To the author’s knowledge, a practical problem that has yet to be addressed in the open literature is the extent to which the SH model can perform well in both OE and CD tests (thus, the calibration is possible) for different types of sands. While the SH model in the first calibration on the Hochstetten’s sand by von Wolffersdorff [37, 25] performed satisfactorily in all tests, many authors have reported on the limits of this model in predicting the volumetric deformations in the CD tests for other sands [41, 13, 17]. In this work, we study these limits and the conflicting requirements on the model parameter to predict stresses and strain in the CD test.

Building upon an extensive exploration of the parameter space via GA, this work aims to investigate the SH model capabilities to describe the 12 OE and 25 CD tests¹ on the Karlsruhe sands published in [42]. Moreover, with the adaptive weighted sum approach to multiobjective optimization [14], we analyze the relationship between the SH model parameters and the model performances in the CD tests. The analysis was carried out using the software GA-cal, an open-source software recently released by the authors [23] for solving the inverse problem of calibrating a constitutive law. The source code of GA-cal, a Fortran revisited version of the algorithms initially developed in Python [25], is freely available at <https://github.com/FraJoMen/GA-cal>.

The article is organized as follows. Section 2 recalls the calibration problem, while Section 3 describes the dataset and the preprocessing. Section 4 presents the calibration results and Section 5 collects the conclusions.

2. The SH Calibration Problem

The SH model proposed by [37] links the time derivative of the Cauchy effective stress \mathbf{T} and the void ratio e , with the granulate stretching rate \mathbf{D} and the state variable e and \mathbf{T} . This link depends on eight parameters; hence the SH model in the OE and CD test case can be written as a system of parametric nonlinear Ordinary Differential Equations (ODEs) as

$$\dot{\mathbf{X}} = \mathbf{H}(\mathbf{X}; \mathbf{P}); \mathbf{X}(0) = \mathbf{X}_0, \quad (1)$$

where $\mathbf{X} = [\mathbf{T}; e]$ is the state vector and \mathbf{P} is the set of parameters:

$$\mathbf{P} = \{e_{c0}, e_{d0}, e_{i0}, h_s, \varphi_c, n, \alpha, \beta\}. \quad (2)$$

The reader is referred to appendix A for more details on this model.

¹The data set is downloadable from the website www.torsten-wichtmann.de/

For the scopes of this work, it suffices to recall that the model calibration consists in identifying the parameters \mathbf{P} that make the trajectory of the system $\mathbf{X}(t)$ match with a set of experimental data $\mathbf{X}(t_k)$ available on a discrete set of times $k = 1, \dots, n_t$.

The experimental results are given in the plane (σ_v, e) for the OE test, with σ_v the effective vertical pressure, and in the triaxial deviatoric (ε_a, q) and triaxial volumetric $(\varepsilon_a, \varepsilon_v)$ planes for the CD test, with q the deviatoric stress, and ε_a and ε_v the volumetric and the axial deformations.

Following the approach proposed in [25], the calibration aims to find the parameters that minimise a cost function. This cost function $C(\mathbf{P})$ measures the discrepancy between model prediction and available data. As in [25], we define it as:

$$C(\mathbf{P}) = w_1 \delta_1(\mathbf{P}) + w_2 \delta_2(\mathbf{P}) + w_3 \delta_3(\mathbf{P}), \quad (3)$$

where w_i weights the discrepancy in each plane on the model performance evaluation (σ_v, e) , (ε_a, q) and $(\varepsilon_a, \varepsilon_v)$. The δ_i , with $i = 1, 2, 3$ functions in the (3) are the average Fréchet distances between data and predictions, measured in appropriate dimensionless plans (see [23]).

The weight in the (3) can be used to prioritise the model performance on one plane or the other. In this work, we use these values to study the feasibility of identifying a set performing well on *all* planes and to reveal contrasting requirements.

Using the GA-cal code, we minimise (3) and explore the parameter space (i.e. the set of possible parameters) with Genetic Algorithm (GA) optimisation.

3. Dataset

The selected experimental data were collected on the *Karlsruhe fine sand*. This sand is characterised by the subangular shape of most grains and no fines content, a mean grain size $d_{50} = 0.14$ mm and a uniformity coefficient $C_u = d_{60}/d_{10} = 1.5$ [42].

The initial conditions for the OE tests are reported in Table 1, while the initial conditions for the CD tests are reported in Table 2. These tables also report the initial relative densities of the samples I_{D0} .

$$I_{D0} = \frac{e_{max} - e_0}{e_{max} - e_{min}}. \quad (4)$$

The minimum and maximum void ratios $e_{min} = 0.677$ and $e_{max} = 1.054$ were determined from standard tests at mean pressure $p = 0$ [42].

3.1. Pre-processing and Test Grouping

To speed up the cost function evaluation (and hence allow for better exploration of the parameter space), the calibration is not carried out on the full data set. Instead, a sub-sampling

Table 1. Oedometric compression tests. The void ratios e_0 and relative densities I_{D0} are measured at the initial conditions.

Test No.	e_0 [-]	I_{D0} [-]
OE1	1.039	0.04
OE2	1.029	0.07
OE3	0.99	0.17
OE4	0.971	0.22
OE5	0.946	0.28
OE6	0.908	0.39
OE7	0.846	0.55
OE8	0.833	0.59
OE9	0.808	0.65
OE10	0.777	0.73
OE11	0.74	0.83
OE12	0.721	0.88

Table 2. Drained monotonic triaxial compression tests. The void ratios e_0 and relative densities I_{D0} are measured at the initial mean pressure p_0 , prior to shearing.

Test No.	e_0 [-]	I_{D0} [-]	p_0 [kPa]
CD1	0.996	0.15	50
CD2	0.975	0.21	100
CD3	0.975	0.21	200
CD4	0.97	0.22	300
CD5	0.96	0.25	400
CD6	0.88	0.46	50
CD7	0.862	0.51	100
CD8	0.859	0.52	200
CD9	0.848	0.55	300
CD10	0.847	0.55	400
CD11	0.84	0.57	50
CD12	0.819	0.63	100
CD13	0.824	0.63	200
CD14	0.822	0.64	300
CD15	0.814	0.68	400
CD16	0.743	0.82	50
CD17	0.758	0.79	100
CD18	0.748	0.81	200
CD19	0.734	0.85	300
CD20	0.753	0.8	400
CD21	0.734	0.85	50
CD22	0.735	0.85	100
CD23	0.706	0.92	200
CD24	0.697	0.95	300
CD25	0.718	0.89	400

was carried out by interpolating the available data. 10 points were uniformly distributed between 10 and 400 kPa for the OE test, while 15 points were uniformly distributed between

points between $\varepsilon_a = 0.01\%$ and $max(\varepsilon_a)$.

The significant sub-sampling drastically reduced the computational time with a negligible loss in accuracy, given the model predictions' smoothness.

To analyse the robustness of the model calibration, the large number of experimental tests were divided into six groups characterised by different initial relative densities I_{D0} . Among the initial conditions identifying each test, the initial void ratio was found to be the one that most influenced the model calibration. The different groups, labelled G1, G2,..., G6 are listed in Table 3. These also differ in the number of tests.

Table 3. Groups of experimental data were used in the calibrations.

Groups labels	Tests	Tests numbers
G1	OE	1, 2, ..., 12
	CD	1, 2, ..., 25
G2	OE	3, 4
	CD	1, 2, ..., 5
G3	OE	6, 7
	CD	6, 7, ..., 10
G4	OE	8, 9
	CD	11, 12, ..., 15
G5	OE	10, 11
	CD	16, 17, ..., 20
G6	OE	11, 12
	CD	21, 22, ..., 25

All input files, output files and the Python scripts for post-processing used in this work are made available in the folder *Example* in the GA-cal repository <https://github.com/FraJoMen/GA-cal>.

4. Results

This section is divided into two parts. In the first (Sec. 4.1), we analyse the GA calibrations on the previously defined groups to study the range of validity of each calibration and its sensitivity to the available data. In the second part (Sec. 4.2), we report on the Pareto front analysis to identify which parameters mostly influence the model performances in the different tests.

4.1. The variability of SH model calibration

For each of the six groups of calibration data sets in Table 3, we consider four sets of weights (w_1, w_2, w_3) (see equation (3)). These are $(1, 1, 1), (1, 0, 0), (0, 1, 0), (0, 0, 1)$; that is, the first gives equal importance to all planes, the second only focuses on the (σ_e, e) plane, the third on the (ε_a, q) plane, etc.

Table 4 reports a set of 24 possible combinations of parameters obtained via GA (labelled as C02, C03, etc) together

with the parameters indicated by Wichtman and Triantafyllidis (WT) [42] (labelled as C01) for reference. For each combination, the table reports the weights used in the cost function and the data group used in the calibration. Moreover, the last column collects the fitness score in (3), weighted by the number of tests n_i in the group used for the calibration and the sum of weights:

$$\eta = \frac{C(\mathbf{P})}{\sum_{j=1}^3 w_j n_i} \quad (5)$$

This normalization enables a fair comparison between parameters that have been evaluated in a different number of planes.

The values of η show that the parameters derived by the GA calibration on all the data (combination C02-C07) outperform the parameter sets by Wichtman and Triantafyllidis (C01) according to the metrics in (3). The error significantly reduces when the calibration focuses on one of the planes. Moreover, the test in group G2 apparently yields the largest error in the $(\varepsilon_a, \varepsilon_v)$ plane.

All these sets of parameters lead to comparable cost functions and can thus be considered ‘optimal’ candidates if evaluated in the data used for their derivation. However, as we shall see shortly, their fitness decreases significantly when evaluated on different data. Moreover, some parameters are more variable than others. This is further illustrated in Table 5, which shows the average value for each parameter, their standard deviation to mean ratio, and their minimum and maximum value. It is thus clear that the parameter h_s, α, β vary significantly among the various calibration, contrary to e_{i0}, e_{d0}, e_{c0} .

To evaluate the accuracy of each set of parameters, we now consider the mean deviation in the abscissa of each plane (σ_v, e) , (ε_a, q) and $(\varepsilon_a, \varepsilon_v)$, normalised by the corresponding maximum variation in the experimental data from each test. That is, given

$$\xi_i = \frac{|Y_{num} - Y_{dat}|}{\max(Y_{dat}) - \min(Y_{dat})} \cdot 100, \quad (6)$$

with Y_{num} the SH model prediction and Y_{dat} the experimentally measured ones, in each plane, we define the global deviation as

$$\xi = \mathbb{E}(\xi_i), \quad (7)$$

where, \mathbb{E} is the expectation operator.

Although this fitness measurement is less suited than the Fréchet distance for calibration purposes because it evaluates the model errors only in one of the axes in each plane, it allows for a more intuitive evaluation of the model performances in relation to the data variability. Indicatively, $\xi \leq 20\%$ is acceptable for the CD test and $\xi \leq 30\%$ for the OE test.

The SH model performances using all the sets in Table 4 is illustrated in detail in Figure 1. The x axis provides the ID of each test and the plane in which the deviation ξ is measured. The first 12 IDs are given to the OE tests, evaluated in the (σ_v, e) plane. The IDs from 12 to 37 are given to the CD tests evaluation in the (ε_a, q) plane, while the last IDs, from 37 to 62, are given to the CD tests evaluated in the plane $(\varepsilon_a, \varepsilon_v)$.

For each test, the upper portion of the graph indicates the minimum and the maximum deviation together with the associated parameter combination. The bottom portion of the graph shows the envelope of performances for all combinations, together with some illustrative cases. No combination reaches the minimal error in all planes. For the OE tests, ξ varies from 3.0 to 189.6 %, for the CD it varies from 3.1 to 181.1 %, in the (ε_a, q) plane and from 1.6 to 210.9 %, in the $(\varepsilon_a, \varepsilon_v)$ plane.

For example, the combination C12 provides excellent results in the CD in the (σ_v, e) , with $\xi \in [4, 30.7]\%$ and mean 14.5%, but fails in both (ε_a, q) and $(\varepsilon_a, \varepsilon_v)$ planes. Not surprisingly, the GA obtained this combination when the weights were set to $(1, 0, 0)$. The trends for the combinations C03 and C20 are also shown using green and red lines in Figure 1. The combination C20 performs well in the plane $(\varepsilon_a, \varepsilon_v)$ with an $\xi \in [3.7, 17.7\%]$ and mean 7.9%, while the combination C03 perform well in the plane (ε_a, q) and $\xi \in [3.9, 21.0\%]$ and mean 8.5%. While this is in line with the choice of weights for C20 and C12, the combination C03 gave equal weights to all planes, thus showing that the amount and the kind of data used for the training play an important role. Figure 2 provides a qualitative overview of the good agreement between the experimental data and the numerical prediction with the combinations C12, C03 and C20.

As shown in Figure 3, some experiments (CD11, CD12, CD13) can be well described with a single set of parameters (C05). We have $\xi \in [2.5, 23.4]\%$, with a mean of 9.1%, for these tests.

Figure 1 also shows the average percentage deviation for the SH using the model parameters by Wichtman and Triantafyllidis (WT) [42] (combination C01) and for the combination C02, which was derived using all the dataset and giving all planes equal importance. Both C01 and C02 perform worst than the optimal combinations in each test, and the comparison shows that C01 favours the model accuracy in the planes (σ_v, e) and (ε_a, q) over the ones in the plane $(\varepsilon_a, \varepsilon_v)$.

To further illustrate the performances of the different combinations, Figures 6 and 7 plot the experimental data together with the model predictions using the best combination on that specific set (black dashed lines) and the predictions using the parameters by Wichtman and Triantafyllidis (C01, with the blue dotted line). While all the identified optimal combinations outperform C01, the improvement comes at the cost of considering a different set of parameters for each test.

The relative importance of model accuracy in these planes

Table 4. Summary of the optimal (calibrated) SH model parameter using GA-cal (C02,C03,...,C25), together with the ones identified by Wichtman and Triantafyllidis (C01). The table also collects the weights w_i , $i = 1, 2, 3$ and the group (see Table 3) used for the calibration as well as the fitness score η (see equation 5).

ID	w_1	w_2	w_3	Group	φ_c	h_s	n	e_{d0}	e_{c0}	e_{i0}	α	β	η
					(°)	(GPa)	(-)	(-)	(-)	(-)	(-)	(-)	(%)
C 01	-	-	-	-	33.10	4.00	0.27	0.672	1.050	1.208	0.14	2.50	2.09
C 02	1	1	1	G1	32.58	4.03	0.28	0.636	1.060	1.219	0.28	1.50	1.21
C 03	1	1	1	G2	32.94	2.27	0.29	0.621	1.070	1.220	0.18	1.33	1.02
C 04	1	1	1	G3	32.91	4.18	0.30	0.616	1.080	1.231	0.20	1.44	0.94
C 05	1	1	1	G4	31.97	2.94	0.31	0.626	1.080	1.188	0.29	1.30	0.88
C 06	1	1	1	G5	31.69	3.83	0.30	0.626	1.080	1.210	0.27	1.38	0.78
C 07	1	1	1	G6	31.75	4.63	0.30	0.621	1.070	1.231	0.28	1.34	0.71
C 08	1	0	0	G1	35.36	6.90	0.27	0.557	0.960	1.142	0.28	1.82	0.66
C 09	1	0	0	G2	29.75	7.86	0.24	0.559	0.980	1.215	0.29	1.77	0.31
C 10	1	0	0	G3	35.37	5.33	0.30	0.545	0.940	1.137	0.28	1.83	0.32
C 11	1	0	0	G4	25.32	7.50	0.30	0.553	0.970	1.213	0.10	1.17	0.52
C 12	1	0	0	G5	29.04	7.54	0.25	0.614	1.040	1.300	0.27	1.71	0.24
C 13	1	0	0	G6	29.50	5.76	0.27	0.589	1.070	1.295	0.22	1.70	0.29
C 14	0	1	0	G1	33.70	3.65	0.24	0.587	1.030	1.174	0.23	1.43	0.81
C 15	0	1	0	G2	34.75	1.94	0.22	0.581	1.020	1.183	0.21	1.55	0.49
C 16	0	1	0	G3	35.21	1.45	0.25	0.586	1.010	1.141	0.21	1.35	0.62
C 17	0	1	0	G4	33.14	3.22	0.27	0.593	1.040	1.144	0.25	1.38	0.97
C 18	0	1	0	G5	32.79	4.86	0.23	0.593	1.040	1.175	0.26	1.41	0.61
C 19	0	1	0	G6	33.21	3.45	0.25	0.571	1.020	1.183	0.26	1.36	0.67
C 20	0	0	1	G1	37.63	2.25	0.30	0.625	1.060	1.177	0.29	1.52	1.05
C 21	0	0	1	G2	38.06	3.61	0.29	0.605	1.080	1.145	0.21	1.26	2.67
C 22	0	0	1	G3	38.96	2.87	0.30	0.583	1.080	1.210	0.22	1.26	0.75
C 23	0	0	1	G4	38.15	4.08	0.33	0.610	1.070	1.220	0.24	1.39	0.61
C 24	0	0	1	G5	37.02	2.35	0.34	0.609	1.050	1.260	0.26	1.78	0.82
C 25	0	0	1	G6	37.38	3.89	0.30	0.615	1.060	1.240	0.25	1.83	0.59

Table 5. Statistics of the obtained parameters. Mean (μ), standard deviation (σ) over mean, minimum and maximum.

Par.	μ	$\sigma/\mu \cdot 10^2$	min	max	
φ_c	(°)	33.65	9.7	25.32	38.96
h_s	(GPa)	4.18	42.7	1.45	7.86
n	(-)	0.28	11.0	0.22	0.34
e_{d0}	(-)	0.60	4.9	0.55	0.67
e_{c0}	(-)	1.04	3.9	0.94	1.08
e_{i0}	(-)	1.20	3.7	1.14	1.30
α	(-)	0.24	20.1	0.10	0.29
β	(-)	1.53	18.6	1.17	2.50

depends significantly on the application. For example, in the slope stability analysis, one is more interested in the accurate modelling of the soil response in the plane (ε_a, q) , and the combination C03 could suit that purpose. On the other hand, in the settlement prediction of a shallow foundation, one is primarily interested in the soil response in the plane $(\varepsilon_a, \varepsilon_v)$, and hence combination C06 could be more appropriate.

In problems such as soil-structure interaction, where the behaviour in all planes are equally relevant, one must accept a compromise (see combination C02) and use a set of coefficients that is sub-optimal in each plane taken separately. The main conclusion in this analysis is that the model calibration in these three planes yields contrasting objectives that bring the SH model to its limits. We search for the parameters driving the compromise in the following section.

4.2. The Pareto Front

The analysis of the combination C01 and C02, aimed at modelling the soil response in all planes, shows that the main discrepancies occurs in the planes (ε_a, q) and $(\varepsilon_a, \varepsilon_v)$, in that the success in one of them yields failure in the other.

In this section, we further analyse the performances in these two planes and identify which parameters are mostly involved in the conflicting requirements. Specifically, we treat the calibration as a multi-objective optimisation which seeks to minimise the average Fréchet distances in these two planes, i.e. δ_2 and δ_3 in (3). We then search for the optimal trade-offs

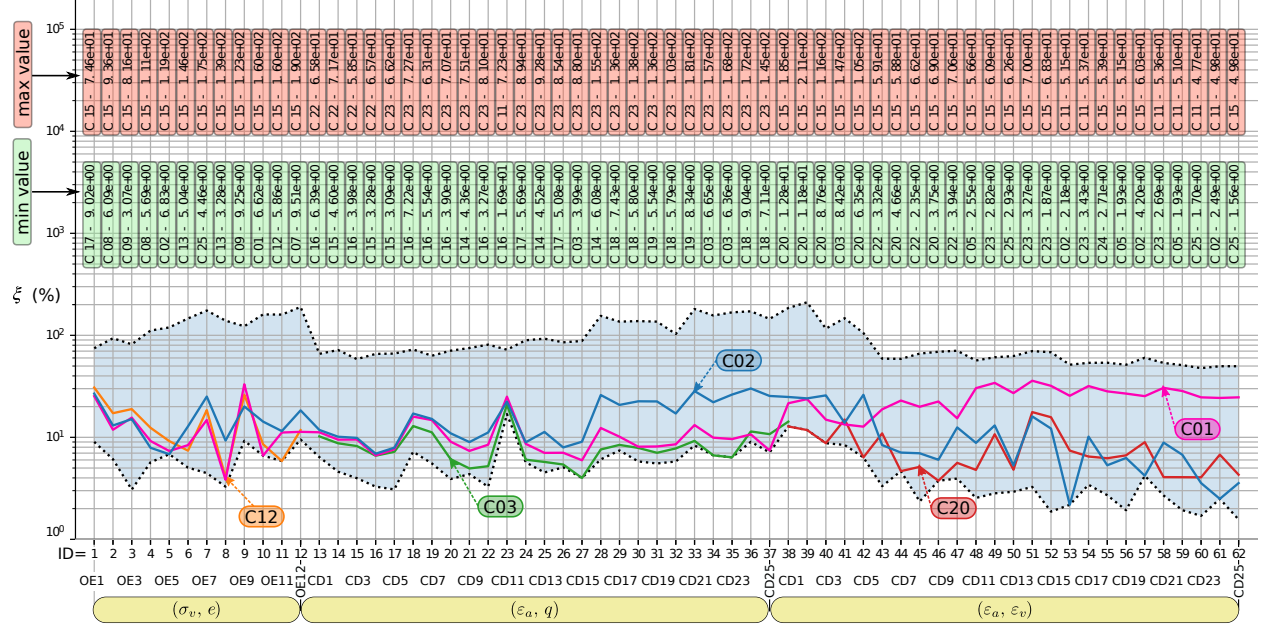


Figure 1. Average percentage deviation ξ (7) in all the OE and CD test data (Tables 1 and 2) considered in this work. The abscissa recalls the test ID and the plane at which the deviation is measured. The combinations providing the best and worst performances for each test are recalled at the top. In the graph, the dashed area in light blue (delimited by black dashed lines) is the envelope of performances for all the combinations of parameters in Table 4). The performance of some illustrative combinations is also reported. The blue, orange, green and red lines are associated with the combinations C15, C12, C03, C20, respectively. These combinations excel in some planes (e.g. C15 and C20 in the second plane, C12 in the first plane, etc.) but fail in others.

between the two objectives, i.e. the Pareto front [4] for the problem. At the Pareto front, improvements in one plane cannot be attained without worsening in the other.

The search for the Pareto front was conducted using the weighted sum method [14]. This approach consists in performing a large set of single objective optimisations (in this case, 400) using weights defined as

$$(1, w_p, 1) \quad \text{and} \quad (1, 1, w_p) \quad (8)$$

where w_p is a vector of linearly spaced values from 0 to 10 with 200 elements. For each calibration, we monitor the values of δ_2 and δ_3 , averaged over the 25 tests in Table 2. The results are plotted in Figure 4, with markers coloured by two of the eight parameters in the optimal set obtained by the calibration: α and φ_c .

The Pareto front is qualitatively identified. Furthermore, the marker face colour allows us to reveal whether any of these parameters changes monotonically from one extreme of the front to the other, and is thus potentially correlated with the degradation of performances in one plane (and the consequent improvement in the other).

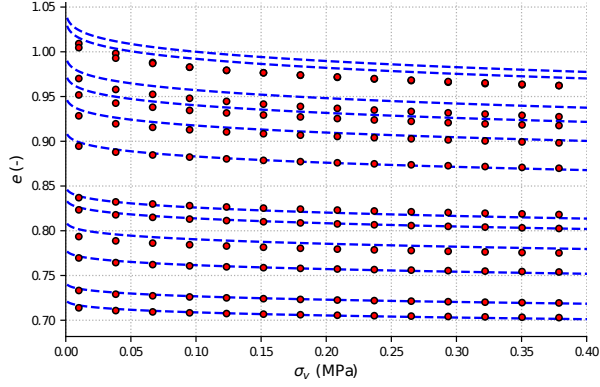
The parameter α was included because this is often considered to be the main responsible for the poor performances in the (ε_v, q) plane and is usually calibrated to reproduce the peak stress rather than the volumetric deformation [41, 13, 17]. However, the plot in Figure 4a display

no clear trend along the Pareto front and thus does not support this common belief. Similar observations holds for the other parameters h_s , n , β , e_{i0} , e_{c0} and e_{d0} , which are thus not shown.

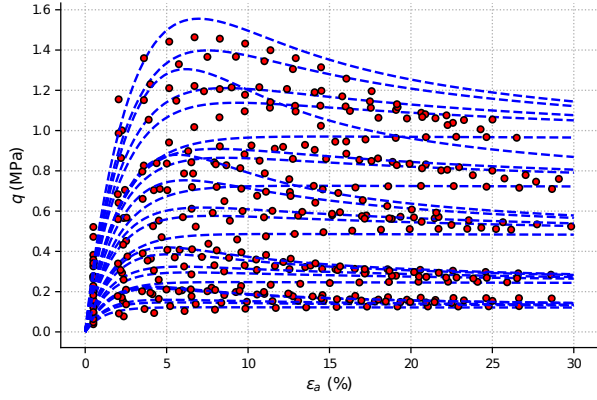
On the other hand, φ_c increases when moving from low δ_2 (high δ_3) to high δ_2 (low δ_3). Relatively low values of φ_c , in the range of 32-35 degrees, produce good predictions of the stress (low values of δ_2) but poor predictions in the strain (large values of δ_3). The opposite is true at the largest values of φ_c , in 36-39 degrees range.

Wu *et al.* [45] have shown that the SH model oversimplifies the constitutive law in [44] and yields an unrealistic relation between the initial Poisson ratio ν_i and the friction angle at critical state φ_c . We here further explore (and corroborate) the reasons for Wu *et al.* [45]'s concerns. Figure 5 plots the initial Poisson ratio ν_i , computed a posteriori from the calibrated curves, and the GA calibrated critical state φ_c for the 400 choices of weights that lead to the Pareto front identification. The different initial conditions (see Table 2) are made visible using different markers for the initial mean pressure p_0 and a colour scale for the void ratios e_0 . The analysis confirms Wu *et al.* [45]'s observation on the link between ν_i and φ_c and complements it with the critical role of the initial conditions: the mean pressure p_0 becomes particularly important for low values of void ratios.

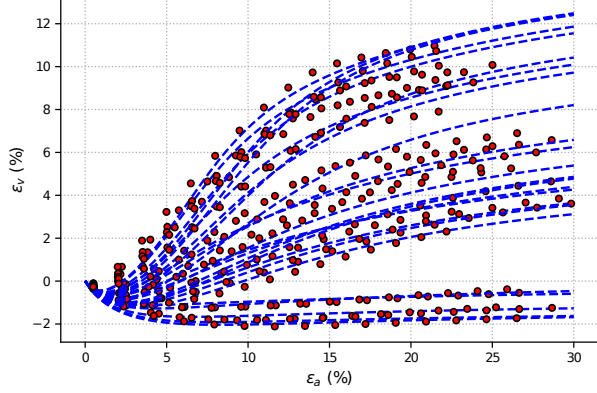
Moreover, the analysis confirms that the SH model yields



(a) Oedometric plane



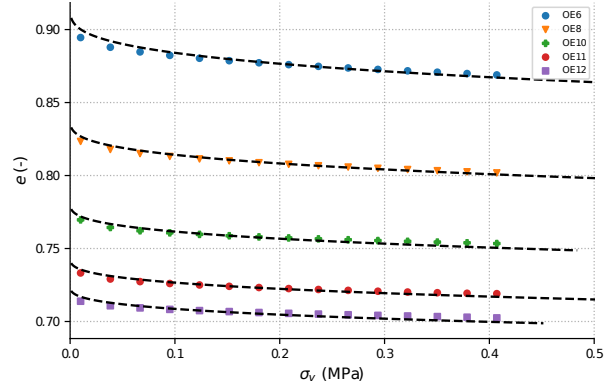
(b) Triaxial deviatoric plane



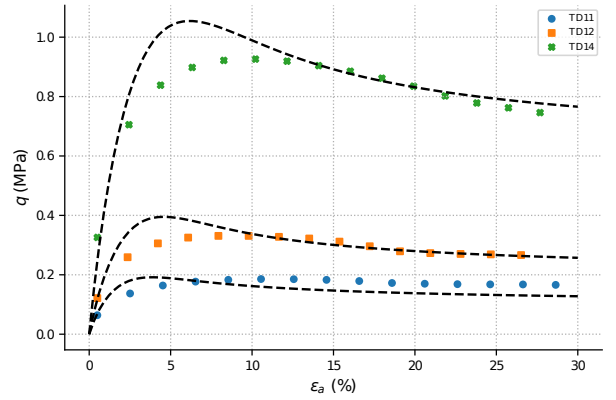
(c) Triaxial volumetric plane

Figure 2. Calibration of the SH model for the individual planes. The figures display the curves obtained with the combination C12, C03 and C20 in the three different planes (a),(b), and (c). These three combinations accurately interpret the results for the 12 OE and 25 CD tests.

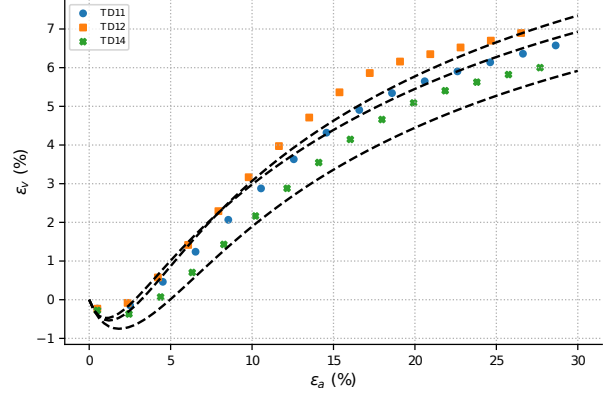
nonphysical negative values for ν_i at large values of φ_c , while the parameter α appears entirely uncorrelated from ν_i . The range 36-39 degrees for φ_c is the one that yields the best model predictions in the $(\varepsilon_a, \varepsilon_v)$ plane. Therefore, the non-physical values of ν_i appear to be necessary for the SH model to overcome its underlying simplification, trading the accuracy in the prediction of the initial (contractile) phases with



(a) Oedometric plane



(b) Triaxial deviatoric plane



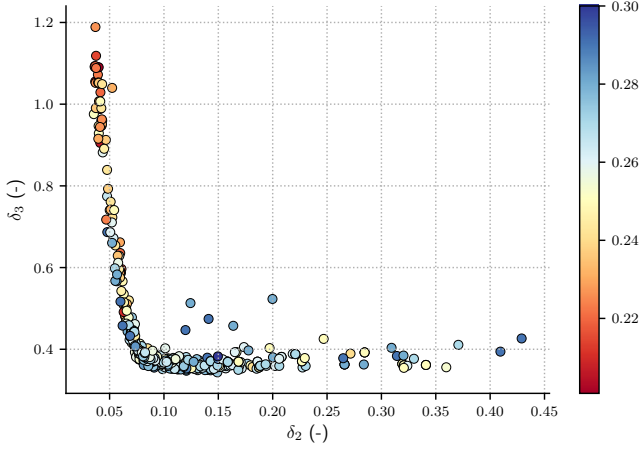
(c) Triaxial volumetric plane

Figure 3. Performance of the SH model in the simultaneous description of CD and OE tests. The figures display the curves obtained with the combination C05. With this combination, we get a good result in all three planes simultaneously for the (CD11, CD12, and CD13).

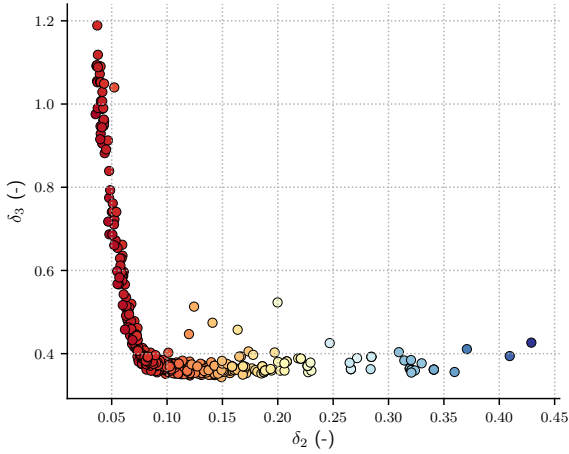
the accurate prediction of the expansion at the largest values of ε_v .

5. Conclusions

We studied the calibration of the SH constitutive law [37] in the 12 OE, and 25 CD tests on the Karlsruhe sands Wicht-



(a) Pareto front (δ_2, δ_3) coloured with α

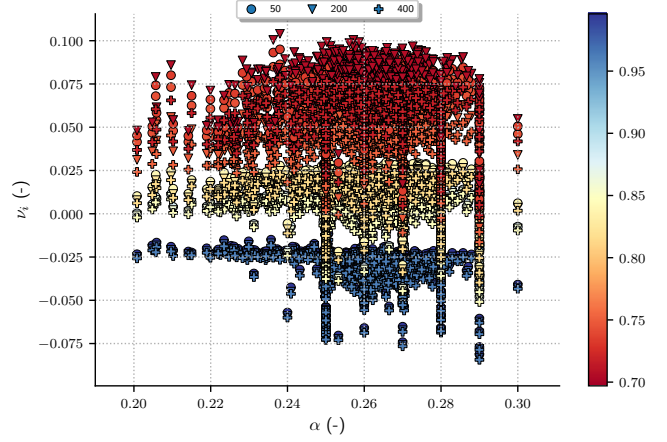


(b) Pareto front (δ_2, δ_3) coloured with φ_c .

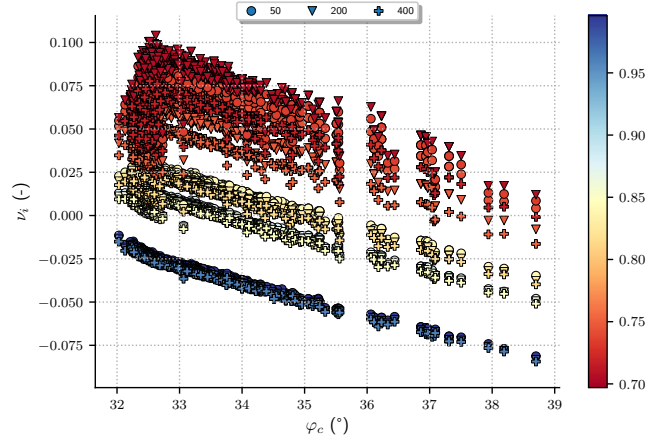
Figure 4. Search for the Pareto front in the minimisation of δ_2 (model performances in the (ε_a, q) plane) and δ_3 (model performances in the $(\varepsilon_a, \varepsilon_v)$ plane). The marker's location is computed by averaging the errors on the 25 tests. These are coloured with the calibrated value for α (a), φ_c (b) and e_{d0} (c).

man and Triantafyllidis [42]. The parameter space was extensively explored using GA [23], by setting the calibration problem in the optimisation framework proposed in [25]. In this framework, the calibration involves identifying the model parameter set that optimises a global performance measure. This is a weight-ed average of model performances in the (σ_v, e) , (ε_a, q) and $(\varepsilon_a, \varepsilon_v)$ planes so that acting on the set of weights it is possible to prioritise accuracy on one plane over the others and study how the model parameters control the model performances.

The available data were divided into six groups. In each of these, the model was calibrated using four combinations of weights to obtain twenty-four sets of optimal parameters. The analysis of the average relative deviation for each combination across the full dataset confirms that the SH model can



(a) ν_i versus the parameters α



(b) ν_i versus the parameters φ_c

Figure 5. Plot of the initial Poisson ratio ν_i versus the parameters α (a), and φ_c (b). The figures highlight the impact of the initial conditions: different markers are used for the initial pressure p_0 while the colour scale in the marker's face refers to the initial void ratio e_0 (see table 2).

be made sufficiently versatile to interpret all the tests, but only if a different set of parameters is used for each. Moreover, a calibration that gives equal weight to all planes provides parameters that perform significantly worse than those obtained when the focus is narrowed to two or even one of the planes. This confirms the need for a compromise in the calibration, particularly in the prediction accuracy for stresses and deformations in the CD tests.

We analysed the conflicting objectives in this compromise using a Pareto front analysis and identified the parameters primarily responsible for it. Contrary to the common belief that this compromise is ruled by the parameter α [41, 13, 17], it was found that the trade-off in prediction accuracy for stresses and deformations in the CD tests is primarily due to the parameter φ_c .

As previously highlighted by Wu *et al.* [45], this parameter is tightly linked to the initial Poisson ratio ν_i , which becomes unrealistically close to zero and eventually negative at the large values of φ_c required to obtain good prediction in the $(\varepsilon_a, \varepsilon_v)$ plane. Furthermore, it was shown that the initial conditions strongly influence the relation between φ_c and ν_i , and negative values of ν_i are obtained for smaller φ_c in the samples with the highest void ratio e_0 .

In conclusion, we have shown that the SH model can be used to predict the soil response in the (σ_v, e) , (ε_a, q) and $(\varepsilon_a, \varepsilon_v)$ planes if the focus is placed on each of these separately. Therefore, the SH model provides enough flexibility to study geotechnical problems such as slope stability or settlement prediction of a shallow foundation, which do not demand high accuracy in *all* planes simultaneously. However, the model performances are inherently limited for problems challenging it in all planes, such as soil structure interaction. The inevitable compromises needed in the calibration have been tightly linked to the parameter φ_c and thus to ν_i .

Conflict of interest

The authors declare no conflict of interest.

A. The SH model

In the formulation of SH by von Wolffersdorff [37], the objective Zaremba-Jaumann [8] stress tensor $\overset{\circ}{\mathbf{T}}$ is:

$$\overset{\circ}{\mathbf{T}} = \frac{f_e f_b}{\text{tr}(\hat{\mathbf{T}}^2)} \left(F^2 \mathbf{D} + a^2 \text{tr}(\hat{\mathbf{T}} \cdot \mathbf{D}) \hat{\mathbf{T}} + f_d a F (\hat{\mathbf{T}} + \hat{\mathbf{T}}^*) \|\mathbf{D}\| \right) \quad (9)$$

where $\|\cdot\|$ is the tensor norm $\|A\| = \sqrt{\text{tr}(AA^T)}$, $\hat{\mathbf{T}}^* = \hat{\mathbf{T}} - 1/3\mathbf{I}$, with \mathbf{I} the identity tensor and $\hat{\mathbf{T}} = \mathbf{T}/\text{tr}(\mathbf{T})$.

$$a = \frac{\sqrt{3}(3 - \sin \varphi_c)}{2\sqrt{2} \sin \varphi_c} \quad (10)$$

$$F = \sqrt{\frac{1}{8} \tan^2 \psi + \frac{2 - \tan^2 \psi}{2 + \sqrt{2} \tan \psi \cos 3\theta} - \frac{\tan \psi}{2\sqrt{2}}}, \quad (11)$$

where:

$$\tan \psi = \sqrt{3} \|\hat{\mathbf{T}}^*\| \quad (12)$$

$$\cos 3\theta = -\sqrt{6} \frac{\text{tr}(\hat{\mathbf{T}}^{*3})}{[\text{tr}(\hat{\mathbf{T}}^{*2})]^{3/2}}. \quad (13)$$

The barotropy coefficients f_b and f_e are:

$$f_b = \frac{\left(\frac{e_{i0}}{e_{c0}}\right)^\beta \frac{h_s}{n} \frac{1+e_i}{e_i} \left(-\frac{\text{tr}(\mathbf{T})}{h_s}\right)^{1-n}}{3 + a^2 - a\sqrt{3} \left(\frac{e_{i0} - e_{d0}}{e_{c0} - e_{d0}}\right)^\alpha}, \quad (14)$$

$$f_e = \left(\frac{e_c}{e}\right)^\beta. \quad (15)$$

The pyknотropy coefficient f_d is defined as

$$f_d = \left(\frac{e - e_d}{e_c - e_d}\right)^\alpha. \quad (16)$$

The maximal (e_d), minimal (e_i) and critical (e_c) void ratio are linked by the system:

$$\frac{e_i}{e_{i0}} = \frac{e_d}{e_{d0}} = \frac{e_c}{e_{c0}} = \exp \left[-\left(\frac{-\text{tr}(\mathbf{T})}{h_s}\right)^n \right]. \quad (17)$$

The materials parameters $\mathbf{P} = \{e_{c0}, e_{d0}, e_{i0}, h_s, \phi, n, \alpha, \beta\}$ are:

- e_{c0} , e_{d0} , e_{i0} . These are, respectively, the critical the minimal and the maximal void ratios, obtained when $p_s = \text{tr}(\mathbf{T}) = 0$ in (17).
- h_s is called granular hardness, and Its increasing increases stiffness and dilatancy.
- φ_c is the critical friction angle at the critical state.
- n is a parameter influencing the barotropy of the soil, influencing the stiffness, peak resistance and dilatancy.
- α is the exponent in the calculation of the pyknотropy coefficient f_d and controls the dependency of peak friction angle on relative density.
- β is a coefficient influencing barotropy and pyknотropy. Increasing β produces an increase of the stiffness of material and in particular the shear stiffness.

The reader is referred to [10, 22, 25] for more details on these parameters, and to [25, 24] for more details on the model formulation and the relevant simplifications related to the OD and CD tests.

Acknowledgements

The authors gratefully acknowledge the support and the discussions with the engineer Pierantonio Cascioli, from GEINA srl, and Gabriele Sandro Toro, laboratory technician of the Department of Engineering and Geology of the Faculty Gabriele D'Annunzio of Chieti.

References

- [1] E. Bauer. Calibration of a comprehensive hypoplastic model for granular materials. *Soils and foundations*, 36(1):13–26, 3 1996.
- [2] Tadikonda Venkata Bharat, Puvvadi V. Sivapullaiah, and Mehter M. Allam. Swarm intelligence-based solver for parameter estimation of laboratory through-diffusion transport of contaminants. *Computers and Geotechnics*, 36(6):984–992, 2009.
- [3] Monia Calista, Antonio Pasculli, and Nicola Sciarra. Reconstruction of the geotechnical model considering random parameters distributions. *Engineering Geology for Society and Territory*, 2:1347–1351, 01 2015.
- [4] Carlos M. Fonseca and Peter John Fleming. An overview of evolutionary algorithms in multiobjective optimization. *Evolutionary Computation*, 3:1–16, 1995.
- [5] W. Fuentes and Th. Triantafyllidis. Isa model: A constitutive model for soils with yield surface in the intergranular strain space. *International Journal for Numerical and Analytical Methods in Geomechanics*, 39(11):1235–1254, 2015.
- [6] W. Fuentes, T. Triantafyllidis, and A. Lizcano. Hypoplastic model for sands with loading surface. *Acta Geotechnica*, 7(3):177–192, Sep 2012.
- [7] W. Fuentes, T. Wichtmann, M. Gil, and C. Lascarro. ISA-hypoplasticity accounting for cyclic mobility effects for liquefaction analysis. *Acta Geotechnica*, 15(6):1513–1531, Jun 2020.
- [8] L. Gambirasio, G. Chiantoni, and E. Rizzi. On the consequences of the adoption of the zaremba–jaumann objective stress rate in fem codes. *Archives of Computational Methods in Engineering*, 23(1):39–67, October 2014.
- [9] G. Gudehus. A comprehensive constitutive equation for granular materials. *Soils and Foundations*, 36(1):1–12, 1996.
- [10] I. Herle and G. Gudehus. Determination of parameters of a hypoplastic constitutive model from properties of grain assemblies. *Mechanics of Cohesive-frictional Materials*, 4(Issue 5):461–486, September 1999.
- [11] A.A Javadi, R Farmani, V.V Toropov, and C.P.M Snee. Identification of parameters for air permeability of shotcrete tunnel lining using a genetic algorithm. *Computers and Geotechnics*, 25(1):1–24, 1999.
- [12] Tomáš Kadlíček, Tomáš Janda, Michal Šejnoha, David Mašín, Jan Najser, and Štěpán Beneš. Automated calibration of advanced soil constitutive models. part i: hypoplastic sand. *Acta Geotechnica*, 17(8):3421–3438, Aug 2022.
- [13] Tomáš Kadlíček, Tomáš Janda, Michal Šejnoha, David Mašín, Jan Najser, and Štěpán Beneš. Automated calibration of advanced soil constitutive models. part ii: hypoplastic clay and modified cam-clay. *Acta Geotechnica*, 17(8):3439–3462, Aug 2022.
- [14] I. Y. Kim and O. L. de Weck. Adaptive weighted sum method for multiobjective optimization: a new method for pareto front generation. *Structural and Multidisciplinary Optimization*, 31(2):105–116, Feb 2006.
- [15] Qitong Li and Zhehao Zhu. Calibration of an elastoplastic model of sand liquefaction using the swarm intelligence with a multi-objective function. *Journal of Rock Mechanics and Geotechnical Engineering*, 2022.
- [16] Emir José Macari, Prasad Samarajiva, and Wije Wathugala. Selection and calibration of soil constitutive model parameters using genetic algorithms. In *Soil Constitutive Models*, pages 310 – 332, Reston, VA, Jan. 2005. American Society of Civil Engineers.
- [17] Jan Machaček, Patrick Staubach, Carlos Eduardo Grandas Tavera, Torsten Wichtmann, and Hauke Zachert. On the automatic parameter calibration of a hypoplastic soil model. *Acta Geotechnica*, Aug 2022.
- [18] J. Machaček, P. Staubach, M. Tafli, H. Zachert, and T. Wichtmann. Investigation of three sophisticated constitutive soil models: From numerical formulations to element tests and the analysis of vibratory pile driving tests. *Computers and Geotechnics*, 138:104276, 2021.
- [19] D. Mašín. A hypoplastic constitutive model for clays. *International Journal for Numerical and Analytical Methods in Geomechanics*, 29(4):311–336, 2005.
- [20] D. Mašín. Clay hypoplasticity with explicitly defined asymptotic states. *Acta Geotechnica*, 8(5):481–496, 2013.
- [21] D. Mašín. Clay hypoplasticity model including stiffness anisotropy. *Géotechnique*, 64(3):232–238, 2014.
- [22] D. Mašín. The influence of experimental and sampling uncertainties on the probability of unsatisfactory performance in geotechnical applications. *Géotechnique*, 65:897–910, 2015.
- [23] Francisco José Mendez, Miguel Alfonso Mendez, and Antonio Pasculli. Ga-cal. v0.0.0, 2022.
- [24] Francisco J. Mendez, Miguel A. Mendez, and Antonio Pasculli. The GA-cal software for the automatic calibration of soil constitutive laws: a tutorial and a user manual, 2022.
- [25] Francisco José Mendez, Antonio Pasculli, Miguel Alfonso Mendez, and Nicola Sciarra. Calibration of a hypoplastic model using genetic algorithms. *Acta Geotechnica*, 16(7):2031–2047, Jul 2021.
- [26] Calista Monia, Pasculli Antonio, and Sciarra Nicola. Reconstruction of the geotechnical model considering random parameters distributions. In Giorgio Lollino, Daniele Giordan, Giovanni B. Crosta, Jordi Corominas, Rafiq Azzam, Janusz Wasowski, and Nicola Sciarra, editors, *Engineering Geology for Society and Territory - Volume 2*, pages 1347–1351, Cham, 2015. Springer International Publishing.
- [27] A. Niemunis and I. Herle. Hypoplastic model for cohesionless soils with elastic strain range. *Mechanics of Cohesive-Frictional Materials*, 2:279–299, 1997.
- [28] Surajit Pal, G. Wije Wathugala, and Sukhamay Kundu. Calibration of a constitutive model using genetic algorithms. *Computers and Geotechnics*, 19(4):325–348, 1996.
- [29] A. Papon, Y. Riou, C. Dano, and P.-Y. Hicher. Single-and multi-objective genetic algorithm optimization for identifying soil parameters. *International Journal for Numerical and Analytical Methods in Geomechanics*, 36(5):597–618, 2012.
- [30] A. Pasculli, M. Calista, and N. Sciarra. Variability of local stress states resulting from the application of monte carlo and finite difference methods to the stability study of a selected slope. *Engineering Geology*, 245:370 – 389, 2018.

- [31] A. Pasculli, A. Pugliese, R. W. Romeo, and T. Sanò. The uncertainty in the local seismic response analysis. *AIP Conference Proceedings*, 1020(1):321–328, 2008.
- [32] Patrick Staubach, Jan Machaček, and Torsten Wichtmann. Novel approach to apply existing constitutive soil models to the modelling of interfaces. *International Journal for Numerical and Analytical Methods in Geomechanics*, 46(7):1241–1271, 2022.
- [33] T. Janda T. Kadlčík and M. Šejnoha. Calibration of hypoplastic models for soils. *Applied Mechanics and Materials*, Vol.821:pp. 503–511, 2016.
- [34] T. Janda T. Kadlčík and M. Šejnoha. 24 th international conference engineering mechanics. In *Automatic online calibration software excalibre*, pages pages 353 – 356, Svratka, Czech Republic, May 14 –17 2019.
- [35] M. Tafili and T. Triantafyllidis. AVISA: anisotropic visco-isa model and its performance at cyclic loading. *Acta Geotechnica*, 15(9):2395–2413, Sep 2020.
- [36] Sotirios Vardakos, Marte Gutierrez, and Caichu Xia. Parameter identification in numerical modeling of tunneling using the differential evolution genetic algorithm (dega). *Tunnelling and Underground Space Technology*, 28:109–123, 2012.
- [37] P.-A. von Wolffersdorff. A hypoplastic relation for granular materials with a predefined limit state surface. *Mechanics of Cohesive-frictional Materials*, 1(3):251–271, 1996.
- [38] Chengwu Wang, Huasheng Sun, Jihua Zhang, and Yu Lu. Influence of foundation pit excavation on tunnels at different locations. *Shock and Vibration*, 2022:4282253, Jan 2022.
- [39] S. Wang and W. Wu. A simple hypoplastic model for overconsolidated clays. *Acta Geotechnica*, Aug 2020.
- [40] Shun Wang and Wei Wu. Validation of a simple hypoplastic constitutive model for overconsolidated clays. *Acta Geotechnica*, Nov 2020.
- [41] Torsten Wichtmann and Theodoros Triantafyllidis. An experimental database for the development, calibration and verification of constitutive models for sand with focus to cyclic loading: part I—tests with monotonic loading and stress cycles. *Acta Geotechnica*, 11(4):739–761, Aug. 2016.
- [42] Torsten Wichtmann and Theodoros Triantafyllidis. An experimental database for the development, calibration and verification of constitutive models for sand with focus to cyclic loading: part II—tests with strain cycles and combined loading. *Acta Geotechnica*, 11(4):763–774, Aug. 2016.
- [43] Wei Wu, Erich Bauer, and Dimitrios Kolymbas. Hypoplastic constitutive model with critical state for granular materials. *Mechanics of Materials*, 23(1):45 – 69, 1996.
- [44] W. Wu and D. Kolymbas. Numerical testing of the stability criterion for hypoplastic constitutive equations. *Mechanics of Materials*, vol. 9:245–253, 1990.
- [45] W. Wu, J. Lin, and X. Wang. A basic hypoplastic constitutive model for sand. *Acta Geotechnica*, 12:1373–1382, 2017.
- [46] M. Yazdani, A. Daryabari, A. Farshi, and S. Talatahari. Application of Taguchi method and genetic algorithm for calibration of soil constitutive models. *Journal of Applied Mathematics*, 2013:258721, Dec 2013.
- [47] Zhen-Yu Yin, Yin-Fu Jin, Jack Shuilong Shen, and Pierre-Yves Hicher. Optimization techniques for identifying soil parameters in geotechnical engineering: Comparative study and enhancement. *International Journal for Numerical and Analytical Methods in Geomechanics*, 42(1):70–94, 2018.
- [48] Zhen-Yu Yin, Yin-Fu Jin, Shui-Long Shen, and Hong-Wei Huang. An efficient optimization method for identifying parameters of soft structured clay by an enhanced genetic algorithm and elastic–viscoplastic model. *Acta Geotechnica*, 12(4):849–867, Aug 2017.
- [49] R. Zentar, P.Y. Hicher, and G. Moulin. Identification of soil parameters by inverse analysis. *Computers and Geotechnics*, 28(2):129–144, 2001.
- [50] Y. Zhang, D. Gallipoli, and C.E. Augarde. Simulation-based calibration of geotechnical parameters using parallel hybrid moving boundary particle swarm optimization. *Computers and Geotechnics*, 36(4):604–615, 2009.
- [51] B. D. Zhao, L. L. Zhang, D. S. Jeng, J. H. Wang, and J. J. Chen. Inverse analysis of deep excavation using differential evolution algorithm. *International Journal for Numerical and Analytical Methods in Geomechanics*, 39(2):115–134, 2015.
- [52] Xinyu Zhao, Joshua Schorr, Andrés Alfonso Peña Olarte, and Roberto Cudmani. A step towards quantifying the uncertainty of the soil mechanical response through the use of genetic algorithms. In Marco Barla, Alice Di Donna, Donatella Sterpi, and Alessandra Insana, editors, *Challenges and Innovations in Geomechanics*, pages 263–271, Cham, 2023. Springer International Publishing.

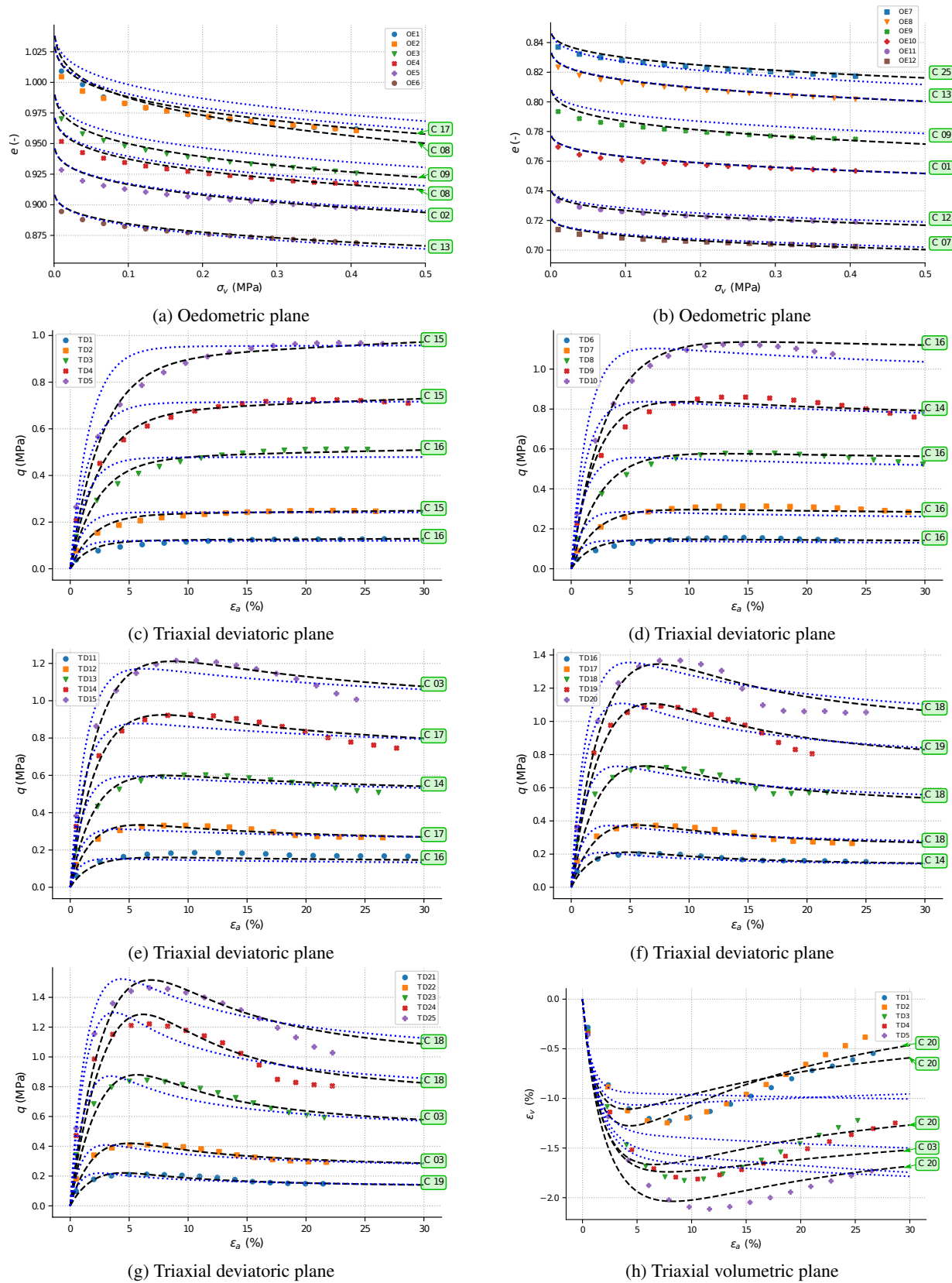
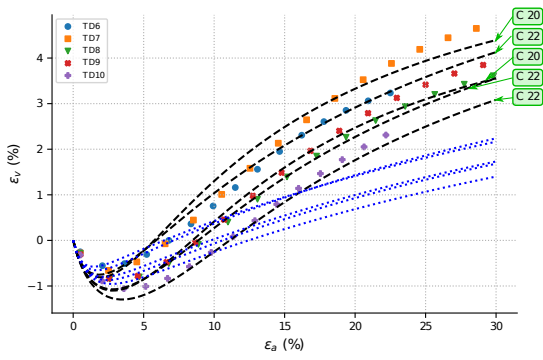
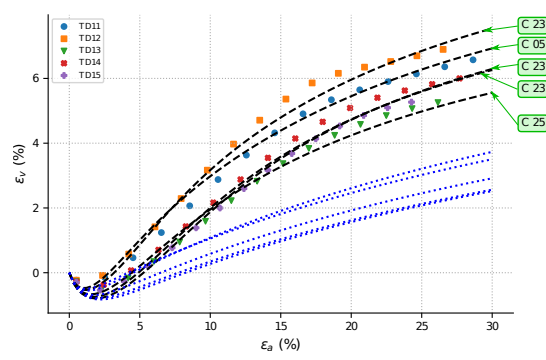


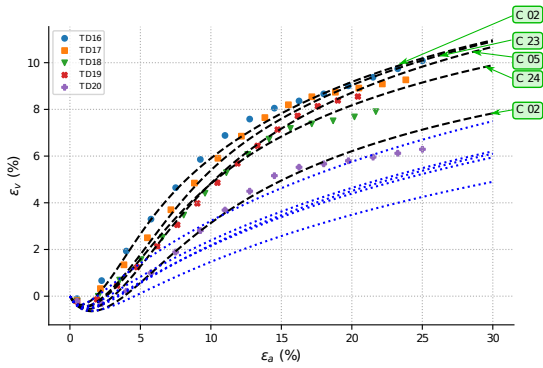
Figure 6. Comparison between the response curves of the SH model and the experimental data (point). The blue dotted lines are computed using the parameters by Wichtman and Triantafyllidis (C01), and the black dashed line with the parameters obtained with GA-cal. The label of the curve refers to Table 4 - Part I.



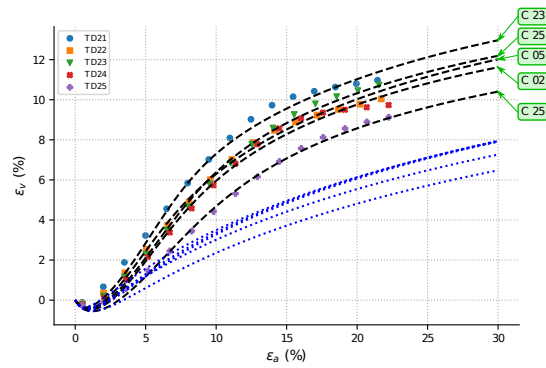
(a) Triaxial volumetric plane



(b) Triaxial volumetric plane



(c) Triaxial volumetric plane



(d) Triaxial volumetric plane

Figure 7. Comparison between the response curves of the SH model and the experimental data (point). The blu dotted lines are computed using Wichtman and Triantafyllidis (C01) parameters, and the black dashed line with the parameters obtained with GA-cal. The label of the curve refers to Table 4 - Part II.